Ultra-Low Complex Blind I/Q-Imbalance Compensation

Thomas Paireder, *Student Member, IEEE*, Christian Motz, *Student Member, IEEE*, Ram S. Kanumalli, Silvester Sadjina, *Student Member, IEEE*, and Mario Huemer, *Senior Member, IEEE*

***Abstract*— Direct-conversion transceivers are the predominating architecture in current mobile communication systems. Despite many advantages, this topology suffers from unavoidable mismatches in the analog part, which causes imbalance between the in-phase and quadrature (I/Q) component. In this paper, we present a novel fully digital, blind I/Q imbalance compensation algorithm that features extremely low computational complexity and high compensation performance for a wide range of input signal types. Different to many state-of-the-art compensation schemes, the approach is not based on a gradient descent optimization and does not require any global feedback. This simplifies the implementation at high data rates and reduces the configuration effort to a minimum. For comparison, we examine an existing method of moment-based estimator with similar properties, for which we also provide the detailed insights beyond available literature. For both algorithms, we provide a rigorous mathematical analysis, which is supported by simulations with a focus on various long-term evolution (LTE) signal types. In addition, hardware architectures, including field-programmable gate array (FPGA) verification, are presented for both algorithms.**

***Index Terms*— Amplitude and phase imbalance, image attenuation, long-term evolution, direct conversion transceiver, field-programmable gate array.**

I. Introduction

CURRENT radio frequency (RF) transceivers implementing mobile communication standards such as Long-Term Evolution (LTE) usually employ the direct-conversion architecture. One big advantage of this architecture is its simplicity due to the fact that the RF signal is split into an in-phase (I) and quadrature (Q) path and directly down-converted without the need for any kind of intermediate frequency (IF) stage. On the other hand, analog non-idealities and parameter variations necessarily lead to errors in terms of gain and phase matching between the I- and Q-path, termed I/Q imbalance. This results in a spectral image compromising the quality of the received signal which can be quantized by the so-called image rejection ratio (IRR) [1]–[6]. Carefully designing the analog paths can reduce the problem but never fully mitigate it: some mismatch in the mixers, local oscillator signals, anti-aliasing filters and the analog-to-digital converters (ADCs) will always remain. Typical IRR values of the analog design itself are around 20 dB to 40 dB [4]–[6]. From a system level perspective it is natural to implement further mechanisms to improve the IRR. Here, digital signal processing proved to be a powerful tool, while also profiting from technology shrinking compared to pure analog approaches.

Manuscript received March 15, 2019; revised May 21, 2019; accepted June 18, 2019. Date of publication July 4, 2019; date of current version August 28, 2019. The authors wish to acknowledge DMCE GmbH & Co KG as part of Intel for supporting this work carried out at the Christian Doppler Laboratory for Digitally Assisted RF Transceivers for Future Mobile Communications. The financial support by the Austrian Federal Ministry for Digital and Economic Affairs and the National Foundation for Research, Technology and Development is gratefully acknowledged. This paper was recommended by Associate Editor S. Gupta. *(Corresponding author: Christian Motz.)*

T. Paireder, C. Motz, and S. Sadjina are with Intel DMCE, 4040 Linz, Austria, and also with the Christian Doppler Laboratory for Digitally Assisted RF Transceivers for Future Mobile Communications, Johannes Kepler University Linz, 4040 Linz, Austria (e-mail: thomas.paireder@jku.at; christian.motz@jku.at).

R. S. Kanumalli is with Intel DMCE, 4040 Linz, Austria.

M. Huemer is with the Christian Doppler Laboratory for Digitally Assisted RF Transceivers for Future Mobile Communications, Johannes Kepler University Linz, 4040 Linz, Austria.

Color versions of one or more of the figures in this article are available online at http://ieeexplore.ieee.org.

Digital Object Identifier 10.1109/TCSI.2019.2924285

A. Prior Approaches for I/Q Imbalance Compensation

The existing algorithms can be divided into two groups: training data assisted approaches and blind ones. The first ones usually feature low complexity, however, they rely on pilot symbols [7]–[9]. This especially complicates their usage in multi-mode multi-standard transceivers. Blind methods on the other hand, do not require specifically allocated training data and often are not standard dependent [10]–[13]. Many blind algorithms use adaptive filtering methods [14], [15]. This typically leads to imbalance cancellation schemes that solve quadratic cost functions using a gradient descent approach [16]–[18]. Although these algorithms feature low complexity, many of them require a feedback loop, which complicates the digital design or the integration in a multi standard digital-front end (DFE). The other category of blind concepts applies blind source separation (BSS) techniques, which however suffer from high computational effort [19]. In the context of interference cancellation [20], [21], I/Q imbalance calibration plays a role, too. Mixed signal solutions employ an auxiliary receiver with less stringent requirements than a normal receiver, which often leads to designs, where low IRR is even more an issue [22], [23]. Digital signal processing is then used to improve the IRR [24]. More general algorithms consider a frequency selective imbalance. This becomes important for signals with very large bandwidth [13], [25]. However, the frequency dependent variations of the imbalance are usually low, which allows an approximation by a finite impulse response (FIR) filter with only a few coefficients [26].

B. Proposed Algorithm

In this work we propose a novel blind low-complexity estimation algorithm utilizing a particular property of the phase

distribution of the I/Q imbalance-free signal that is approximately fulfilled by many communication signals. However, the algorithm can also be applied to signals not fulfilling this property. As we will show in a detailed mathematical analysis, the estimator will then be biased. For comparison, we study an existing algorithm [12] that is based on the method of moments [27] and provide detailed insights beyond available literature. The moment-based estimator is derived by assuming the so-called properness [28] of the I/Q-imbalance-free signal. The analytical results are supported by extensive simulations, where we test the algorithms with signals defined by the LTE standard for uplink (UL) and downlink (DL), namely single-carrier frequency-division multiple access (SC-FDMA) and orthogonal frequency-division multiple access (OFDMA). The simulation results clearly show, which signal parameters (such as bandwidth allocation and modulation scheme [29]) have an influence on the compensation performance. One major advantage of both algorithms is that the estimation of the I/Q imbalance can be decoupled from the cancellation itself and thus they are feedback-free in that sense. This makes them highly flexible in the context of mobile communication transceivers that feature already a highly complex DFE. There, integrating new or updated components that require feedback is a demanding task as it requires evaluating mutual influence of all parts at a system level. For both estimators, we develop an efficient low-complexity hardware design, which allows us to compare their capabilities by processing I/Q data from a real RF transceiver within a field-programmable gate array (FPGA). The application on measurement data clearly shows the benefits of the proposed ultra-low complexity estimator, as it performs equivalently to the, theoretically slightly superior, moment-based approach, but requires much less hardware resources, especially no multipliers.

The rest of the paper is organized as follows: In Section II a baseband model for I/Q imbalance is derived. Based on this model, Section III describes an ideal compensation scheme and a corresponding hardware architecture. In Section IV, the ultra-low complexity imbalance estimator is presented, including its mathematical derivation, simulation results and a hardware-efficient implementation. The moment-based estimator is described in Section V, where we extend the existing mathematical analysis and provide extensive simulation results and a hardware architecture. The effect of fixed-point arithmetic on the estimation performance of both algorithms is examined in Section VI. Section VII provides a comparison of the proposed estimator to other state-of-the-art approaches and illustrates the influence of fixed-point arithmetic. The image rejection performance of both algorithms on measured data is shown in Section VIII, followed by concluding remarks in Section IX.

II. Basic I/Q Imbalance Model

Fig. 1 shows the relevant blocks of a direct-conversion RF receiver. In the analog domain, all stages from the antenna to the I/Q-mixer, like switches and a low noise amplifier, operate on the real-valued RF signal. Therefore they have no influence on the imbalance and are omitted in our considerations. The first relevant stage, the I/Q mixer, down-converts the wanted receive signal located around the carrier frequency f_{Rx} to the complex-valued analog baseband. At this point, the analog paths for the in-phase and quadrature component split and the mixer itself already introduces a mismatch between the I- and the Q-signal. Additionally, due to unavoidable parameter variations all subsequent analog circuits up to the analog-to-digital converter contribute to the I/Q-imbalance. In general, this mismatch is frequency-dependent. But as measurements on our targeted receiver show negligible frequency-dependence up to its maximum bandwidth of 20 MHz, in the following we will focus on the frequency-independent case.

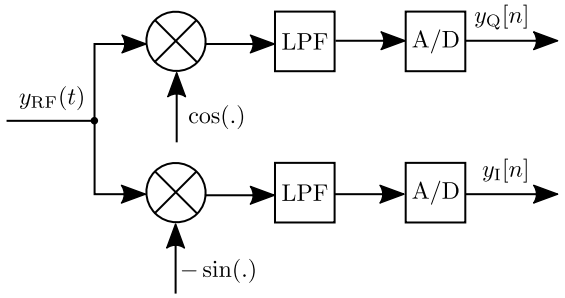

Fig. 1. Basic block diagram of the relevant parts of a direct-conversion RF receiver.

As we intend to compensate the mismatch in the digital domain, we first derive a baseband signal model. Let $\widetilde{x}_{\mathrm{BB}}(t)$ be the complex-valued wanted receive signal, then

$$y_{\mathrm{RF}}(t) = \Re\left\{\widetilde{x}_{\mathrm{BB}}(t)\, e^{j2\pi f_{\mathrm{Rx}} t}\right\} \tag{1}$$

represents the RF signal at the input of the mixer. Without loss of generality, the imbalance is commonly assumed to be concentrated at the mixer stage, even though the subsequent analog blocks also contribute as discussed above. The local oscillator signals of the non-ideal mixer are modeled as

$$s_{\mathrm{LO,I}}(t) = \left(1 + \frac{\epsilon_A}{2}\right)\cos\left(2\pi f_{\mathrm{Rx}}\, t - \frac{\epsilon_\theta}{2}\right), \tag{2}$$

$$s_{\mathrm{LO,Q}}(t) = -\left(1 - \frac{\epsilon_A}{2}\right)\sin\left(2\pi f_{\mathrm{Rx}}\, t + \frac{\epsilon_\theta}{2}\right), \tag{3}$$

where ϵ_A and ϵ_θ represent the time-invariant gain and phase mismatch between and the I- and Q-component. The real-valued output signals of the mixer

$$y_{\mathrm{RF,mixer,I}}(t) = y_{\mathrm{RF}}(t) \cdot s_{\mathrm{LO,I}}(t), \tag{4}$$

$$y_{\mathrm{RF,mixer,Q}}(t) = y_{\mathrm{RF}}(t) \cdot s_{\mathrm{LO,Q}}(t) \tag{5}$$

are usually combined to a complex-valued signal

$$\begin{aligned} y_{\mathrm{RF,mixer}}(t) &= y_{\mathrm{RF,mixer,I}}(t) + j\, y_{\mathrm{RF,mixer,Q}}(t) \\ &= y_{\mathrm{RF}}(t) \cdot (s_{\mathrm{LO,I}}(t) + j\, s_{\mathrm{LO,Q}}(t)) \\ &= y_{\mathrm{RF}}(t) \cdot s_{\mathrm{LO}}(t) \end{aligned} \tag{6}$$

with the complex-valued local oscillator signal $s_{\mathrm{LO}}(t)$. The mixer output signal still contains unwanted components around $\pm 2\ f_{\mathrm{Rx}}$. These components are rejected by low pass filters with

a passband gain of $G_{\mathrm{LPF}} = 2$, leading to the analog baseband signal $y_{\mathrm{BB}}(t)$ as follows:

$$\begin{aligned} y_{\mathrm{BB}}(t) &= G_{\mathrm{LPF}} \cdot \mathrm{LPF}\left\{y_{\mathrm{RF,mixer}}(t)\right\} \\ &= G_{\mathrm{LPF}} \cdot \mathrm{LPF}\left\{\frac{1}{2}\left(\widetilde{x}_{\mathrm{BB}}(t)\, e^{j2\pi f_{\mathrm{Rx}} t} + \widetilde{x}^{*}_{\mathrm{BB}}(t)\, e^{-j2\pi f_{\mathrm{Rx}} t}\right)\cdot \right. \\ &\quad \left[\left(1+\frac{\epsilon_A}{2}\right)\cos\left(2\pi f_{\mathrm{Rx}}\, t - \frac{\epsilon_\theta}{2}\right)\right. \\ &\quad \left.\left. -j\left(1-\frac{\epsilon_A}{2}\right)\sin\left(2\pi f_{\mathrm{Rx}}\, t + \frac{\epsilon_\theta}{2}\right)\right]\right\} \\ &= \frac{1}{2}\,\widetilde{x}_{\mathrm{BB}}(t)\left[\left(1+\frac{\epsilon_A}{2}\right)e^{j\frac{\epsilon_\theta}{2}} + \left(1-\frac{\epsilon_A}{2}\right)e^{-j\frac{\epsilon_\theta}{2}}\right] \\ &\quad + \frac{1}{2}\,\widetilde{x}^{*}_{\mathrm{BB}}(t)\left[\left(1+\frac{\epsilon_A}{2}\right)e^{-j\frac{\epsilon_\theta}{2}} - \left(1-\frac{\epsilon_A}{2}\right)e^{j\frac{\epsilon_\theta}{2}}\right] \\ &= k_1\,\widetilde{x}_{\mathrm{BB}}(t) + k_2\,\widetilde{x}^{*}_{\mathrm{BB}}(t). \end{aligned} \tag{7}$$

Here x^* denotes the complex conjugate of x. k_1 and k_2 are defined as

$$k_1 = \frac{1}{2}\left[\left(1+\frac{\epsilon_A}{2}\right)e^{j\frac{\epsilon_\theta}{2}} + \left(1-\frac{\epsilon_A}{2}\right)e^{-j\frac{\epsilon_\theta}{2}}\right], \tag{8}$$

$$k_2 = \frac{1}{2}\left[\left(1+\frac{\epsilon_A}{2}\right)e^{-j\frac{\epsilon_\theta}{2}} - \left(1-\frac{\epsilon_A}{2}\right)e^{j\frac{\epsilon_\theta}{2}}\right]. \tag{9}$$

As the gain and phase mismatches of practically used receiver designs are typically small, $|k_1|$ will be close to 1. As a consequence we define $x_{\mathrm{BB}}(t) = k_1\,\widetilde{x}_{\mathrm{BB}}(t)$ and intend to reconstruct $x_{\mathrm{BB}}(t)$ instead of the true wanted signal $\widetilde{x}_{\mathrm{BB}}(t)$. The remaining gain and phase error on $x_{\mathrm{BB}}(t)$ can then be easily corrected by the channel equalizer, which is present in every wireless communication system. This leads to the analog baseband model

$$y_{\mathrm{BB}}(t) = x_{\mathrm{BB}}(t) + \alpha\, x^{*}_{\mathrm{BB}}(t) + w_{\mathrm{BB}}(t), \tag{10}$$

with $\alpha = \frac{k_2}{k_1^*}$. $\widetilde{w}_{\mathrm{BB}}(t)$ is baseband equivalent additive noise, which comprises thermal and semiconductor-related noise components of the analog circuits after the mixer stage. For the sake of clearness this term has been omitted in the previous derivation steps.

All algorithms presented in the subsequent chapters operate in the digital baseband, therefore we simplify the notation by omitting the subscript. Assuming an ADC that only introduces quantization noise due to finite bit width, the discrete-time imbalance model is

$$y[n] = x[n] + \alpha\, x[n]^{*} + w[n]. \tag{11}$$

$w[n]$ is the total noise, consisting of the sampled component $w_{\mathrm{BB}}(t)$ and the ADC quantization noise. For the sake of clearness, we neglect the additive noise term in all following derivations and simulations, which leads to the simplified model:

$$y[n] = x[n] + \alpha\, x[n]^{*}. \tag{12}$$

In Section VIII we show the imbalance compensation performance on measured data from an integrated LTE receiver to obtain the expectable performance of the proposed algorithms in practically relevant scenarios.

Fig. 2 illustrates the power spectral density (PSD) of a sample signal $y[n]$ with $\alpha = 0.1\, e^{j0.25}$. To ensure clear visibility of the imbalance effect, the sample signal was chosen to only contain components in the negative frequency range. Due to the imbalance, the component $x[n]^*$ in the positive frequency range occurs. Compared to the PSD of $x[n]$, the PSD of $x[n]^*$ is scaled and mirrored at $f = 0$. Therefore the conjugate complex component is usually referred to as *image*.

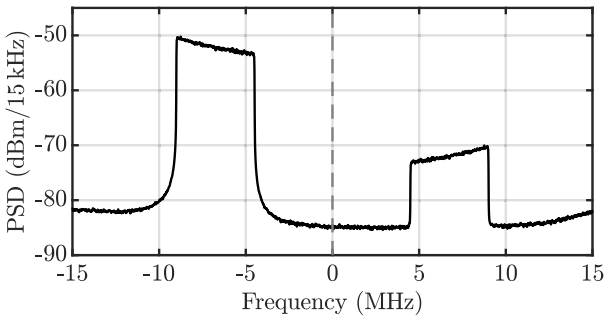

Fig. 2. Example of wanted receive signal and its spectral image for an imbalance factor of $\alpha = 0.1\, e^{j0.25}$.

III. Image Cancellation

The reconstruction of $x[n]$ from the distorted signal $y[n]$ in (12) can be done in a two-step procedure: firstly the estimation of α, and secondly the cancellation of the image in $y[n]$. As the second step can be conducted independently of the estimation algorithm, we first consider the cancellation scheme and provide a hardware architecture for this step.

A. Mathematical Formulation

In the following, we drop the time indices in favor of a shorter notation and rewrite the noise-free model (12) in the real-composite form by splitting x, y, and α into an in-phase and quadrature component, i.e. $x = x_{\mathrm{I}} + j x_{\mathrm{Q}}$, $y = y_{\mathrm{I}} + j y_{\mathrm{Q}}$ and $\alpha = \alpha_{\mathrm{I}} + j\alpha_{\mathrm{Q}}$. The real-composite form of (12) is then:

$$\begin{bmatrix} y_{\mathrm{I}} \\ y_{\mathrm{Q}} \end{bmatrix} = \underbrace{\begin{bmatrix} 1+\alpha_{\mathrm{I}} & \alpha_{\mathrm{Q}} \\ \alpha_{\mathrm{Q}} & 1-\alpha_{\mathrm{I}} \end{bmatrix}}_{\mathbf{T}} \begin{bmatrix} x_{\mathrm{I}} \\ x_{\mathrm{Q}} \end{bmatrix}. \tag{13}$$

With

$$\mathbf{T}^{-1} = \frac{1}{1-\alpha_{\mathrm{I}}^2-\alpha_{\mathrm{Q}}^2}\begin{bmatrix} 1-\alpha_{\mathrm{I}} & -\alpha_{\mathrm{Q}} \\ -\alpha_{\mathrm{Q}} & 1+\alpha_{\mathrm{I}} \end{bmatrix} \tag{14}$$

we have

$$\begin{bmatrix} x_{\mathrm{I}} \\ x_{\mathrm{Q}} \end{bmatrix} = \mathbf{T}^{-1}\begin{bmatrix} y_{\mathrm{I}} \\ y_{\mathrm{Q}} \end{bmatrix}, \tag{15}$$

which leads to

$$x_{\mathrm{I}} = k_{\mathrm{canc}}\left[(1-\alpha_{\mathrm{I}})\, y_{\mathrm{I}} - \alpha_{\mathrm{Q}}\, y_{\mathrm{Q}}\right] \tag{16}$$

$$x_{\mathrm{Q}} = k_{\mathrm{canc}}\left[-\alpha_{\mathrm{Q}}\, y_{\mathrm{I}} + (1+\alpha_{\mathrm{I}})\, y_{\mathrm{Q}}\right]. \tag{17}$$

The scaling factor k_{canc} hereby is

$$k_{\mathrm{canc}} = \frac{1}{1-\alpha_{\mathrm{I}}^2-\alpha_{\mathrm{Q}}^2} = \frac{1}{1-|\alpha|^2}. \tag{18}$$

Combining the components x_I and x_Q to the complex-valued x again yields

$$\begin{aligned} x &= x_\mathrm{I} + j x_\mathrm{Q} \\ &= k_\mathrm{canc} \left[(1-\alpha_\mathrm{I})\, y_\mathrm{I} - \alpha_\mathrm{Q}\, y_\mathrm{Q} - j\alpha_\mathrm{Q}\, y_\mathrm{I} + j(1+\alpha_\mathrm{I})\, y_\mathrm{Q} \right] \\ &= k_\mathrm{canc}\, (y - \alpha\, y^*), \end{aligned} \tag{19}$$

In a practical implementation, α in (18) and (19) will be replaced by the estimate $\hat{\alpha}$, and therefore we will also obtain the estimate

$$\widehat{x} = \widehat{k}_\mathrm{canc}\, (y - \widehat{\alpha}\, y^*). \tag{20}$$

with $\widehat{k}_\mathrm{canc} = \frac{1}{1-|\widehat{\alpha}|^2}$. As a consequence, the image will not be completely suppressed. The power of the remaining image P_img in relation to the power of the wanted signal P_main is quantified by the image rejection ratio (IRR). The logarithmic image rejection ratio IRR_dB of the input signal y without any cancellation is defined as

$$\mathrm{IRR}_\mathrm{dB} = 10 \cdot \log_{10} \frac{P_\mathrm{main}}{P_\mathrm{img}} = 10 \cdot \log_{10} \frac{1}{|\alpha|^2}. \tag{21}$$

After the cancellation we have:

$$\begin{aligned} \widehat{x} &= \widehat{k}_\mathrm{canc}\, ((x + \alpha\, x^*) - \widehat{\alpha}\, (x^* + \alpha^* x)) \\ &= \underbrace{\widehat{k}_\mathrm{canc}\, (1 - \alpha^* \widehat{\alpha})\, x}_{\text{main comp.}} + \underbrace{\widehat{k}_\mathrm{canc}\, (\alpha - \widehat{\alpha})\, x^*}_{\text{image comp.}}. \end{aligned} \tag{22}$$

The IRR after the cancellation is again the power ratio between the main and the image component, which leads to

$$\mathrm{IRR}_\mathrm{dB}^\mathrm{canc} = 10 \cdot \log_{10} \frac{|1 - \alpha^* \widehat{\alpha}|^2}{|\alpha - \widehat{\alpha}|^2}. \tag{23}$$

Without calibration, receiver designs typically achieve an IRR of about 20 dB to 40 dB [4]–[6].

B. Digital Hardware Architecture

For our target application, namely mobile communication systems, the received data have to be processed in real-time. Depending on the desired data rates and the used semiconductor process technology, this might lead to stringent requirements on the digital hardware design. Because of several advantages, we chose to implement a fully pipelined architecture. Inserting register stages between all major arithmetic operations allows to run the design at high clock frequencies or to reduce the area requirements by relaxing the constraints on the adder and multiplier units.

Fig. 3 shows a detailed block diagram of the fully pipelined architecture implementing (19). In a first step, the cancellation $x' = y - \alpha\, y^*$ is performed. It requires 1 adder for the complex conjugation of y, 4 real multipliers and 2 real adders for the complex multiplication $\alpha\, y^*$, and 2 real adders for the subtraction. Full pipelining is achieved with 12 register stages, where the bit width of all registers is equal to the input sample width. In the second step, the gain correction is applied to the canceler output signal x'. The implementation differs from the ideal scaling (18) in one point: the division is very unfavorable for hardware implementation and thus is replaced by an approximation. In practice, we can assume that

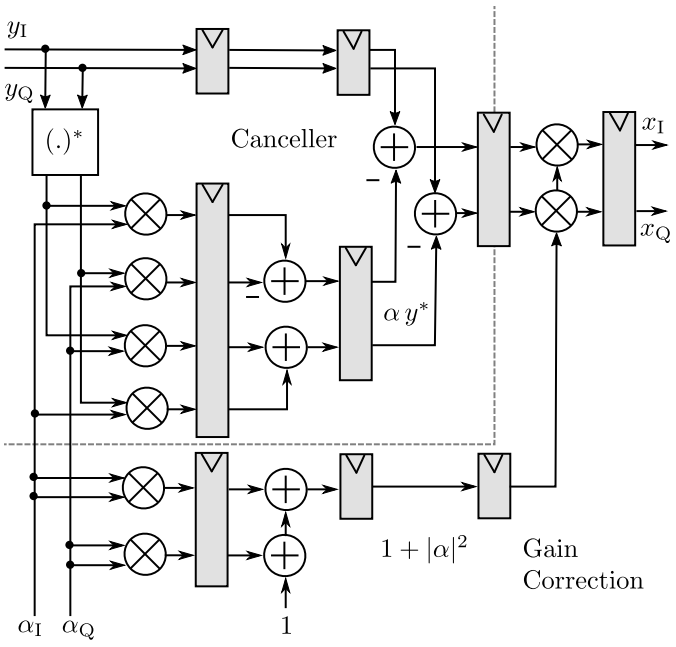

Fig. 3. Fully pipelined hardware architecture for image cancellation.

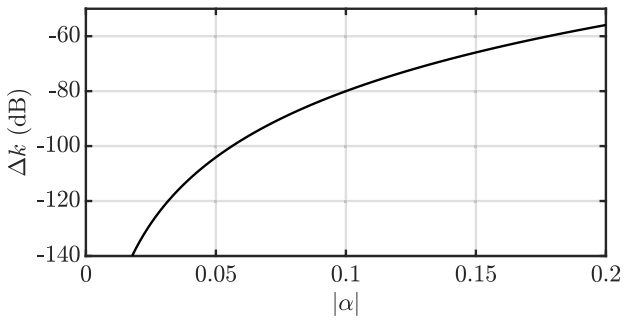

Fig. 4. Deviation between exact scaling factor k_canc and Taylor series approximation $\widetilde{k}_\mathrm{canc}$.

the magnitude of the imbalance factor α is typically below 0.1. Consequently, the factor k_canc or its estimated value $\widehat{k}_\mathrm{canc}$ can be replaced by a first order Taylor series approximation at the point $|\alpha| = 0$.

$$k_\mathrm{canc} = \frac{1}{1-|\alpha|^2} \approx 1 + |\alpha|^2 = \widetilde{k}_\mathrm{canc} \tag{24}$$

Fig. 4 visualizes the normalized approximation error

$$\Delta k_\mathrm{dB} = 10 \cdot \log_{10} \frac{\left|\widetilde{k}_\mathrm{canc} - k_\mathrm{canc}\right|^2}{k_\mathrm{canc}^2} \tag{25}$$

in the relevant range of $|\alpha|$. The maximum deviation is around -55 dB and thus justifies the simplification. As shown in Fig. 3, the implementation of the gain correction part requires 4 real multipliers and 2 real adders. 6 registers are used for pipelining.

The architecture has been synthesized on an Intel Cyclone V FPGA. Tab. I summarizes the resource usage and the maximum clock frequency of the design for the selected device. Inputs, outputs and all internal paths used a 13 bit signed data format. Due to the fully pipelined design, very high clock

TABLE I
RESOURCE USAGE OF IMBALANCE CANCELER ON CYCLONE V 5CSXFC6D6F31C6 FPGA (RELATIVE USAGE IN PARENTHESIS)

	w/o. Gain Correction	w. Gain Correction
Logic Util. (in ALMs)	94 (< 1 %)	149 (< 1 %)
Register Bits	159 (< 1 %)	200 (< 1 %)
Embedded Multipliers	4 (2 %)	8 (4 %)
F_{max} (Slow 1.1 V 85 °C)	300 MHz	213 MHz

frequencies of over 200 MHz are achieved. The number of multipliers allocated by the synthesis is consistent with Fig. 3.

IV. ULTRA-LOW COMPLEXITY IMBALANCE ESTIMATION

As shown in the previous section, the reconstruction of the wanted receive signal is possible if an accurate estimate of the imbalance factor α is available. Typically, applications require a fast adaption speed, high estimation accuracy and low complexity from a hardware implementation perspective. The first estimator presented in this paper focuses on the last requirement and features extremely low complexity. The output of the estimator can directly be supplied to the image cancellation scheme shown in Section III to improve the IRR. In the subsequent sections, we derive the statistical properties of the algorithm, validate the results with simulations and provide synthesis results for an FPGA implementation. Results with measurement data are given in Section VIII.

A. Algorithm and Basic Properties

We consider the noise-free imbalance model (12). To begin with, we examine the (practically irrelevant) special case of $|\alpha| = 1$, where the exact solution can be obtained from a single sample at an arbitrarily chosen time index n:

$$\frac{y[n]}{y[n]^*} = \frac{e^{j\frac{\phi_\alpha}{2}}\left(e^{-j\frac{\phi_\alpha}{2}}\,x[n] + e^{j\frac{\phi_\alpha}{2}}\,x[n]^*\right)}{e^{-j\frac{\phi_\alpha}{2}}\left(e^{j\frac{\phi_\alpha}{2}}\,x[n]^* + e^{-j\frac{\phi_\alpha}{2}}\,x[n]\right)} = e^{j\phi_\alpha} = \alpha. \quad (26)$$

Here the model (12) was inserted and α was converted to polar form. Astoundingly, for $|\alpha| \leq 1$, α equals the mean of the left hand side of (26):

$$\alpha = \mathrm{E}\left[\frac{y[n]}{y[n]^*}\right] = \mathrm{E}\left[e^{j\,2\arg(y[n])}\right], \quad (27)$$

when $x[n]$ fulfills some conditions that we will discuss shortly. Here, E[.] is the expectation operator, arg(.) denotes the argument of a complex number and $y[n]$ is the random signal as defined in (12). As it will be derived in Section IV-B, the equality (27) holds under the condition that the *phase of the wanted signal* $x[n]$ *is uniformly distributed* in the interval $[-\pi, \pi)$. To give practical examples, Fig. 5 visualizes the phase distribution of a fully allocated LTE-20 uplink signal with underlying BPSK,[1] QPSK[2] and 16-QAM[3] constellation mapping as well as a fully allocated LTE-20 BPSK downlink signal. Due to the SC-FDMA modulation scheme used for the uplink, the constellation mapping has direct influence on the phase distribution. Below 16-QAM, the actual distribution differs significantly from the uniformity assumption. Due to the OFDM[4] modulation scheme, for downlink signals, the distribution is uniform for BPSK, too.

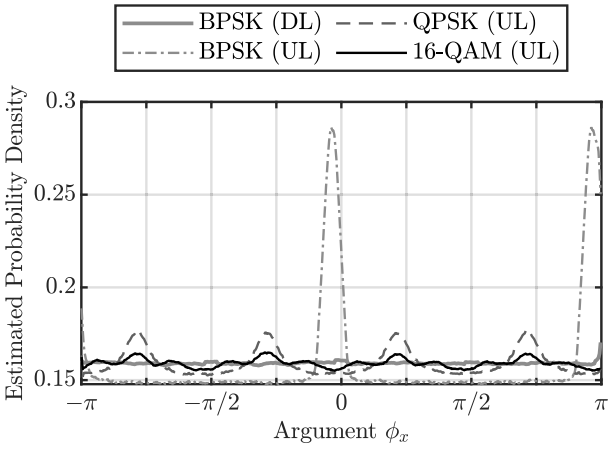

Fig. 5. Comparison of phase distributions of fully allocated LTE-20 uplink and downlink signals with selected modulation types.

(27) requires to calculate an ensemble mean of $e^{j\,2\arg(y[n])}$. Under the assumption that $e^{j\,2\arg(y[n])}$ is ergodic in the mean [30], the natural approximation of the expectation operator is the sample mean. We therefore suggest the following estimator for α:

$$\widehat{\alpha}[n] = \frac{1}{n}\sum_{k=1}^{n}\frac{y[k]}{y[k]^*} = \frac{1}{n}\sum_{k=1}^{n} e^{j\,2\arg(y[k])}. \quad (28)$$

Note that the estimation is independent of the signal power, since the magnitude of $y[n]$ cancels in each individual summand. This also means that each summand represents a point on the unit circle in the complex plane. The mean of these points is solely defined by the phase distribution of the terms $\frac{y[n]}{y[n]^*}$. Each distinct value of α inside the unit circle leads to a unique phase distribution of $y[n]$.

If real-time processing of the incoming data samples is required, the block-based sample mean (28) can be replaced by the iterative version.

$$\begin{aligned}\widehat{\alpha}[0] &= 0\\ \widehat{\alpha}[n] &= \left(1 - \frac{1}{n}\right)\widehat{\alpha}[n-1] + \frac{1}{n}\,e^{j\,2\arg(y[n])}, \quad n = 1, 2, \ldots\end{aligned} \quad (29)$$

This equation already indicates the main advantage of the estimator: its extremely low hardware complexity. The exponential term can be calculated by 2 CORDIC[5] stages [31] and a static bit shift, and therefore requires no multiplications. The constant $\frac{1}{n}$ in (29) can also be well approximated by bit shifts.

[1]Binary Phase Shift Keying
[2]Quadrature Phase Shift Keying
[3]Quadrature Amplitude Modulation
[4]Orthogonal Frequency-Division Multiplexing
[5]Coordinate Rotation Digital Computer

B. Mathematical Analysis

To analyze the statistical properties of the estimator, we start by proofing the equality (27). This equality holds, as asserted above, when the phase of $x[n]$ is uniformly distributed within $[-\pi, \pi)$. By inserting the noise-free model (12) into (27), converting x to polar form and simplifying one yields

$$\mathrm{E}\left[\frac{y}{y^*}\right] = \mathrm{E}\left[\frac{x + \alpha\, x^*}{x^* + \alpha^* x}\right] = \mathrm{E}\left[\frac{e^{j\phi_x} + \alpha\, e^{-j\phi_x}}{e^{-j\phi_x} + \alpha^*\, e^{j\phi_x}}\right]. \quad (30)$$

Here we assumed that the mean does not depend on the time index. With

$$f(\phi_x) = \frac{e^{j\phi_x} + \alpha\, e^{-j\phi_x}}{e^{-j\phi_x} + \alpha^*\, e^{j\phi_x}} \quad (31)$$

the expected value in (30) can be written as integral

$$\mathrm{E}[f(\phi_x)] = \int_{-\pi}^{\pi} f(\phi_x)\, p_\Phi(\phi_x)\, \mathrm{d}\phi_x. \quad (32)$$

Here, $p_\Phi(\phi_x)$ is the probability density function (PDF) of ϕ_x, which is now assumed to be uniform in $[-\pi, \pi)$:

$$p_\Phi(\phi_x) = \begin{cases} \dfrac{1}{2\pi}, & \text{for } \phi_x \in [-\pi, \pi) \\ 0, & \text{else} \end{cases}. \quad (33)$$

In order to analytically evaluate the integral, the substitution $z = e^{-j\phi_x}$ is introduced. Transforming the integration path leads to a contour integral on the unit circle

$$\mathrm{E}[f(\phi_x)] = -\frac{1}{2\pi} \oint_\Gamma f(z) \frac{\mathrm{d}z}{jz} = -\frac{1}{2\pi j} \oint_\Gamma \frac{1 + \alpha\, z^2}{z^3 + \alpha^* z}\, \mathrm{d}z. \quad (34)$$

Because the integration path Γ is a closed curve in the complex plane, Cauchy's residue theorem

$$\frac{1}{2\pi j} \oint_\Gamma f(z)\, \mathrm{d}z = \sum_{k=1}^{n} \mathrm{Ind}_\Gamma(a_k)\ \mathrm{Res}_{a_k}(f). \quad (35)$$

can be applied to solve the definite integral [32]. a_k are isolated singularities inside Γ. $\mathrm{Ind}_\Gamma(a_k)$ is the winding number relative to a_k and is -1 in our case as the curve is traversed once in clockwise – or mathematically negative – direction. $\mathrm{Res}_{a_k}(f)$ are the residues of f at the points a_k. Assuming a_k are simple poles of f, the residues can be calculated as follows:

$$\mathrm{Res}_{a_k}(f) = \lim_{z \to a_k} (z - a_k)\, f(z). \quad (36)$$

For the practically relevant case $|\alpha| < 1$, the integrand in (34) has three poles inside the unit circle, which are $a_1 = 0$, $a_2 = j\sqrt{\alpha^*}$ and $a_3 = -j\sqrt{\alpha^*}$. The corresponding residues are:

$$\mathrm{Res}_{a_1}(f) = \lim_{z \to 0} \frac{z + \alpha\, z^3}{z^3 + \alpha^* z} = \frac{1}{\alpha^*} \quad (37)$$

$$\mathrm{Res}_{a_2}(f) = \lim_{z \to j\sqrt{\alpha^*}} \frac{1 + \alpha\, z^2}{z^2 + j\sqrt{\alpha^*} z} = \frac{|\alpha|^2 - 1}{2\alpha^*} \quad (38)$$

$$\mathrm{Res}_{a_3}(f) = \lim_{z \to -j\sqrt{\alpha^*}} \frac{1 + \alpha\, z^2}{z^2 - j\sqrt{\alpha^*} z} = \frac{|\alpha|^2 - 1}{2\alpha^*}. \quad (39)$$

Combining all intermediate results gives

$$\mathrm{E}\left[\frac{y}{y^*}\right] = \mathrm{E}[f(\phi_x)] = \sum_{k=1}^{n} \mathrm{Res}_{a_k}(f) = \alpha. \quad (40)$$

For $|\alpha| = 1$, as already stated in (26), we have $\alpha = \frac{y[n]}{y[n]^*}$, such that

$$\mathrm{E}\left[\frac{y[n]}{y[n]^*}\right] = \alpha \quad (41)$$

is valid for $|\alpha| \leq 1$, independent of the argument of α.

As stated above, the practical implementation of the estimator is the sample mean (28). Due to the linearity of the expectation operator and by applying the equality (41), the unbiasedness of the proposed estimator under the assumption made on $x[n]$ can easily be shown:

$$\mathrm{E}[\widehat{\alpha}] = \mathrm{E}\left[\frac{1}{n} \sum_{k=1}^{n} \frac{y[k]}{y[k]^*}\right] = \frac{1}{n} \sum_{k=1}^{n} \mathrm{E}\left[\frac{y[k]}{y[k]^*}\right] = \alpha \quad (42)$$

It turns out that a closed form solution for the variance of the estimator cannot easily be found in general. It is, however, possible to find an expression for the variance under the additional assumption that the sequence $\frac{y[n]}{y[n]^*}$ is uncorrelated. This assumption is fulfilled if the sequence $\phi_x[n]$ is independently distributed. Note, that the independence assumption is violated by many communication signals as it will be shown in simulations.

With these assumptions, the sample mean can be interpreted as mean over n individual, uncorrelated estimates $\frac{y[k]}{y[k]^*}$. This allows to split the variance expression as follows:

$$\begin{aligned} \mathrm{Var}[\widehat{\alpha}] &= \frac{1}{n^2} \sum_{k=1}^{n} \mathrm{Var}\left[\frac{y[k]}{y[k]^*}\right] \\ &= \frac{1}{n^2} \sum_{k=1}^{n} \left(\mathrm{E}\left[\left|\frac{y[k]}{y[k]^*}\right|^2\right] - \left|\mathrm{E}\left[\frac{y[k]}{y[k]^*}\right]\right|^2 \right) \\ &= \frac{1}{n^2} \sum_{k=1}^{n} (1 - |\alpha|^2) \\ &= \frac{1}{n} (1 - |\alpha|^2), \end{aligned} \quad (43)$$

where the equality (41) was used. In the special case of $|\alpha| = 1$, (43) yields 0. This result is consistent with (26), since for $|\alpha| = 1$ the exact solution can be obtained from a single sample. Interestingly, the variance is independent of the phase of α.

C. Simulation Results

In the derivation of the unbiasedness (42) we assumed that the phase $\phi_x[n]$ is uniformly distributed, a property which is approximately true for a number of communication signals. However, for the derivation of the variance in (43) we additionally assumed that $\phi_x[n]$ is independently distributed, which is typically not fulfilled for practical communication signals. To verify the theoretical results, we consider simulations with white Gaussian noise at first. We then proceed with signals that violate one or both of the assumptions. 10^5 data samples were

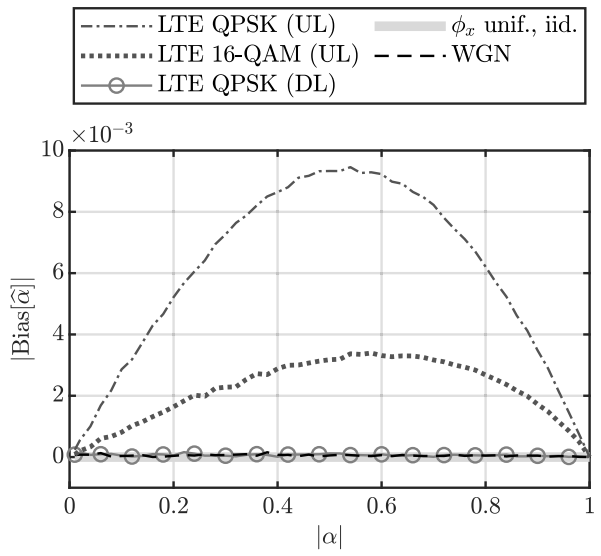

(a)

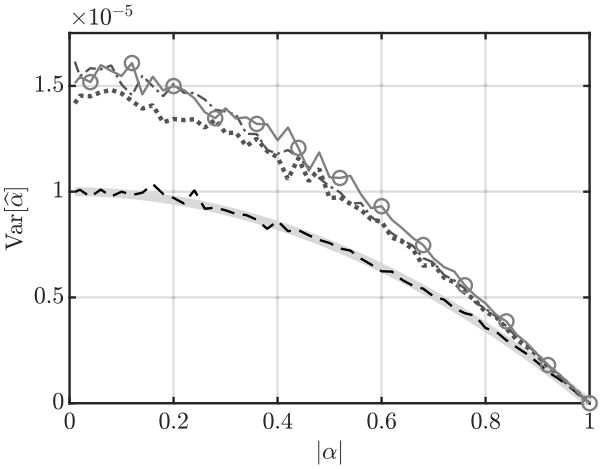

(b)

Fig. 6. Ultra-low complexity estimator: theoretical bias (a) and variance (b) under assumption of uniform and independent distribution of ϕ_x compared to simulations with white Gaussian noise and fully allocated LTE-20 up- and downlink signals (100 resource blocks).

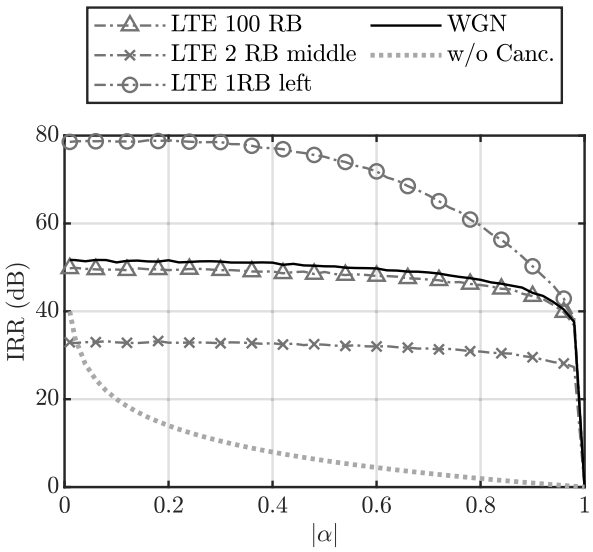

Fig. 7. Ultra-low complexity estimator: Simulated image rejection ratio for white Gaussian noise and LTE-20 downlink signals with three different allocation patterns.

used for all simulations, and the estimator was implemented using double-precision arithmetic.

Fig. 6a shows the simulated bias for white Gaussian noise and fully allocated LTE-20 uplink and downlink signals with QPSK and 16-QAM constellation mapping. Fig. 6b visualizes the corresponding variance and compares it to (43). Both figures show ensemble averages. For white Gaussian noise, the simulation results perfectly match with theory. The bias is zero (except for fluctuations within simulation accuracy) and the variance equals the theoretical result. In contrast to that, the estimator is biased for both LTE uplink signals. The bias is caused by the constellation mapping of the LTE signals, which violates the uniformity assumption on the phase of $x[n]$. As depicted in Fig. 5, the 16-QAM modulation causes less deviation from a uniform distribution than QPSK and consequently shows less bias, too. For the downlink signal, the phase distribution is uniform and the estimator is unbiased, independent of the constellation. Compared to (43), the variance of the estimator is larger by a factor of about 1.5 for both, up- and downlink signals. The reason is that the sequence $\phi_x[n]$ is correlated for LTE signals, which violates the independence assumption made during the derivation of the variance expression.

For the application in a receiver, the most relevant performance metric is the image rejection ratio (23). Fig. 7 depicts the $\mathrm{IRR}_{\mathrm{dB}}^{\mathrm{canc}}$ for selected signal types. Here in addition to the estimation of α, the exact cancellation (20) was applied. The $\mathrm{IRR}_{\mathrm{dB}}$ without cancellation (21) acts as a baseline. Even though the initial $\mathrm{IRR}_{\mathrm{dB}}$ in a receiver is usually above 20 dB (corresponding to $|\alpha| < 0.1$), for simulations α is varied over the full range from 0 to 1 because the results are of interest from a theoretical point of view. For a white Gaussian input signal, the $\mathrm{IRR}_{\mathrm{dB}}^{\mathrm{canc}}$ is almost constant over a wide range of α. A value of 51 dB is achieved for $|\alpha| < 0.6$. In contrast to that, for an LTE downlink signal with QPSK constellation mapping, the $\mathrm{IRR}_{\mathrm{dB}}^{\mathrm{canc}}$ heavily depends on the allocation pattern. Fig. 8 symbolically illustrates the power spectral density of the three allocations, which were used in the simulation. For a single outer left resource block (RB), the $\mathrm{IRR}_{\mathrm{dB}}^{\mathrm{canc}}$ is excellent with about 79 dB in the relevant range $|\alpha| < 0.1$. A fully allocated LTE signal with 100 RBs leads to an $\mathrm{IRR}_{\mathrm{dB}}^{\mathrm{canc}}$ of about 50 dB for $|\alpha| < 0.1$. In case of a centered narrow allocation the $\mathrm{IRR}_{\mathrm{dB}}^{\mathrm{canc}}$ drops to about 32 dB in the relevant range. This allocation type corresponds to a highly oversampled signal with little information gain per sample. In this case, the performance could be enhanced by increasing the sequence length used for estimation. Despite the different modulation type, the performance of the estimator does not differ significantly for LTE uplink signals.

D. Digital Hardware Architecture

As already stated in Section III-B, in this paper, we focus on real-time processing of data streams. Therefore we implemented the iterative sample mean (29) instead of the

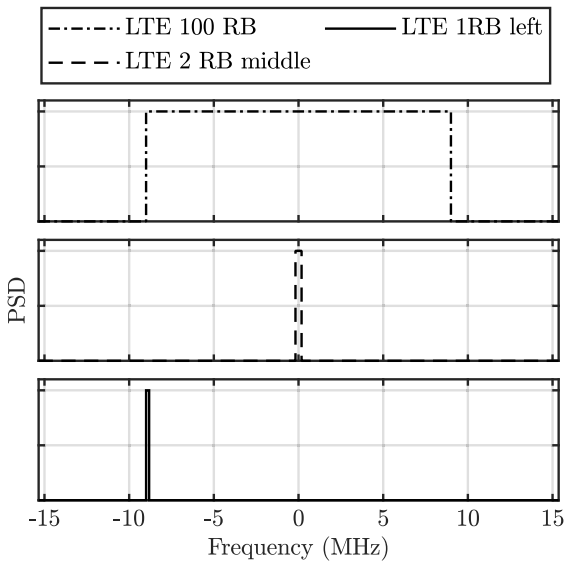

Fig. 8. LTE-20 allocation patterns used for simulation.

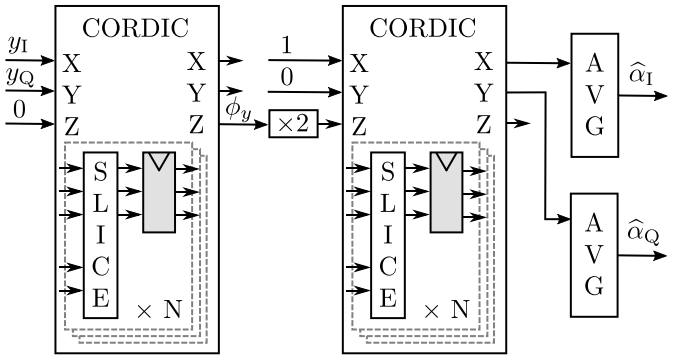

Fig. 9. Top level block diagram of low-complexity estimator.

block-based variant. We present a fully pipelined architecture to relax the timing constraints on the arithmetic operations. Fig. 9 illustrates the basic block diagram of the estimator without cancellation. The first term required by the algorithm is $e^{j2\arg(y[n])}$, which equals a normalization of the sample $y[n]$ followed by a doubling of its phase. The CORDIC algorithm provides a multiplier-less approximation for this kind of vector operations. The CORDIC basically splits the rotation of a vector into hardware efficient partial rotations. A CORDIC slice performs one such partial rotation and requires 3 adders and 2 static shifters. In a first step, we use a parallel CORDIC implementation [31] with 7 slices to rotate the complex input sample towards the real axis. In this so-called vectoring mode, the CORDIC outputs the magnitude and phase of the input sample. We then omit the magnitude and double the phase with a static bit shift. In the next step, we rotate the real value 1 by the doubled phase value using a CORDIC with 7 slices in rotation mode. The result of the second stage is the approximated real and imaginary component of $e^{j2\arg(y[n])}$. Both CORDICs operate on 13 bit signed data and use pipelining registers between all individual slices. The outputs of the second CORDIC stage are passed to two averager stages,

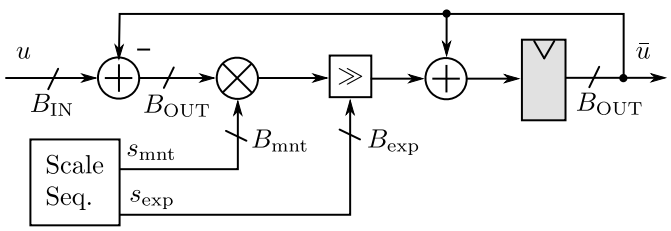

Fig. 10. Fully pipelined hardware architecture of averager.

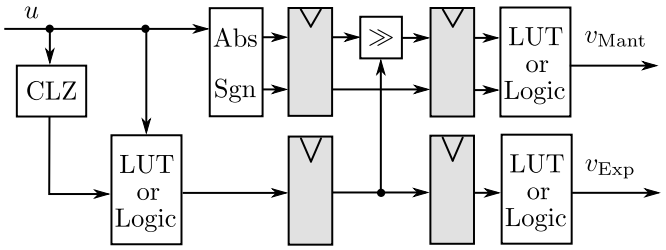

Fig. 11. General lookup table based approximation of nonlinear functions.

which compute the iterative sample mean as shown in Fig. 10. The mean is implemented as follows:

$$\bar{u}[n] = ((u[n] - \bar{u}[n-1]) \cdot s_{\text{mnt}}[n]) \gg s_{\text{exp}}[n] + \bar{u}[n-1], \qquad (44)$$

where $\gg$ denotes a variable arithmetic right shift. Instead of using two multipliers with high bit width as suggested by (29), the proposed structure uses a single multiplier with lower bitwidth and a variable shifter. This custom floating-point representation increases the dynamic range of the scaling factor. Nonetheless, the computation of the scaling factor $\frac{1}{n}$ requires a computationally intensive division in each time step. A rough, but hardware efficient approximation of the division is to replace $\frac{1}{n}$ entirely by bit shifts, i. e. $s_{\text{mnt}}[n] = 1$ and $s_{\text{exp}}[n] = \lfloor \log_2(n) \rfloor$, where $\lfloor . \rfloor$ is the floor function. The sequence of shift values could be efficiently computed on the fly or stored in a relatively small table. If the accuracy of this approximation is not sufficient, another possibility is to evaluate the division by using a small lookup table (LUT). Fig. 11 shows a general architecture capable of computing any nonlinear function through lookup tables. To keep the lookup table small, the input value is first converted into a custom floating point format. Afterwards, the mantissa, the exponent and the sign are processed separately by means of a lookup table or other logic. At the output, sign and mantissa are combined again. Depending on the represented function, the logic manipulating the exponent might be very simple. In case of the division, just a sign change is required. Intuitively, the LUT based iterative sample mean is considerably more accurate for short input sequences (below 1000 samples) or certain signal types. For random signals or when averaging over longer sequences, the difference in the approximation error reduces.

The algorithm depicted in Fig. 9 has been synthesized on a Cyclone V FPGA. Both, the shift based and the LUT based approximation of the division have been implemented. Tab. II shows the resource requirements and the maximum achievable clock frequencies. At maximum, this estimator

TABLE II
RESOURCE USAGE OF LOW-COMPLEXITY IMBALANCE ESTIMATOR ON CYCLONE V 5CSXFC6D6F31C6 FPGA (RELATIVE RESOURCE USAGE IN PARENTHESIS)

	Avg. w. Shifts	Avg. w. LUT
Logic Util. (in ALMs)	955 (2 %)	1163 (4 %)
Register Bits	572 (< 1 %)	669 (< 1 %)
Embedded Multipliers	0 (0 %)	2 (< 1 %)
F_{max} (Slow 1.1 V 85 °C)	112 MHz	72 MHz

requires 2 multipliers and a very low number of logic elements. Therefore, its area and power requirements are minimal.

V. IMBALANCE ESTIMATION BASED ON METHOD OF MOMENTS

For comparison, in this paper we examine a second estimator, which was first published in [12], and give valuable insights beyond existing literature. The estimator is based on a standard method of statistics: the method of moments [27]. Like the algorithm presented in Section IV, this algorithm can directly be combined with the imbalance compensation scheme in Section III to improve the IRR. However, it can also be used as a standalone estimator. In the following, we repeat the derivation for later reference, provide a comprehensive performance evaluation for different signal types and develop an appropriate hardware architecture.

A. Algorithm and Basic Properties

We base the derivation again on the noise-free model (12). As the estimator operates on a complex-valued input sequence $y[n]$, the theory for complex random variables and signals is applied in the derivation. Particularly, it requires the so-called properness of complex-random variables. For a zero mean random variable z, properness is given when [28]:

$$\mathrm{E}[z^2] = 0. \tag{45}$$

or equivalently

$$\mathrm{E}[z_\mathrm{I}^2] = \mathrm{E}[z_\mathrm{Q}^2] \tag{46}$$

$$\mathrm{E}[z_\mathrm{I}\, z_\mathrm{Q}] = 0 \tag{47}$$

We now assume that the samples of the *wanted signal* $x[n]$ *are zero mean and proper*. Note that this property holds for communications signals with square-type constellation, like QPSK, 16-QAM, etc. Additionally we assume that the variances of the real and imaginary part of $x[n]$, σ_I^2 and σ_Q^2, are independent of the time index. Then σ_I^2 and σ_Q^2 are equal and from now on denoted with $\sigma_{x_\mathrm{I,Q}}^2$. Note that due to the zero mean assumption on $x[n]$, the imbalance signal $y[n]$ is also zero mean.

The method of moments starts by expressing the relevant moments of the true distribution of a random variable by analytic functions in k unknown parameters. In our case the unknowns are the power $\sigma_{x_\mathrm{I,Q}}^2$ of the real or imaginary part of $x[n]$ and the imbalance factor α. The required moments are the variance and the pseudo-variance of the complex random signal $y[n]$. While the former is equal to the power of $y[n]$, the latter is a measure for the properness of the signal. As $y[n]$ is assumed to be zero mean, the moments are:

$$m_1 = \mathrm{E}[|y[n]|^2] = 2\,(1 + |\alpha|^2)\,\sigma_{x_\mathrm{I,Q}}^2 \tag{48}$$

$$m_2 = \mathrm{E}[y[n]^2] = 4\,\alpha\,\sigma_{x_\mathrm{I,Q}}^2. \tag{49}$$

This system of independent equations can be solved for $\sigma_{x_\mathrm{I,Q}}^2$ and α. The solutions are:

$$\sigma_{x_\mathrm{I,Q}}^2 = \frac{1}{4}\left(m_1 + \sqrt{m_1^2 - |m_2|^2}\right) \tag{50}$$

$$\alpha = \frac{m_2}{4\,\sigma_{x_\mathrm{I,Q}}^2}. \tag{51}$$

Assuming that $|y[n]|^2$ and $y[n]^2$ are ergodic in the mean, again the natural approximation of the ensemble means are the sample means. Therefore, the following estimates are used for m_1 and m_2:

$$\widehat{m}_1[n] = \frac{1}{n}\sum_{k=1}^{n} |y[k]|^2 \tag{52}$$

$$\widehat{m}_2[n] = \frac{1}{n}\sum_{k=1}^{n} y[k]^2, \tag{53}$$

which in turn can be replaced by the iterative forms

$$\widehat{m}_1[0] = 0, \quad \widehat{m}_2[0] = 0$$

$$\widehat{m}_1[n] = \left(1 - \frac{1}{n}\right)\widehat{m}_1[n-1] + \frac{1}{n}\,|y[n]|^2 \tag{54}$$

$$\widehat{m}_2[n] = \left(1 - \frac{1}{n}\right)\widehat{m}_2[n-1] + \frac{1}{n}\,y[n]^2 \tag{55}$$

if block-based processing is not applicable. The estimator $\hat{\alpha}$ for α is consequently given by inserting (54) and (55) into (50) and (51).

Due to the complexity of the occurring terms, the bias and variance of the estimator cannot easily be derived analytically. However, simulations (see Section V-C) indicate that the estimator is unbiased for proper signals $x[n]$ with zero mean.

B. Complex Exponential Input Sequence

In all previous considerations, we limited the assumptions on the wanted signal $x[n]$ to a minimum as the aim was to develop a blind estimation algorithm applicable for typical communication signals. But as an extension to the existing literature, we now apply the idea of the moment-based estimator to complex exponential sequences. This special deterministic signal has high similarity to a single-carrier of multi-carrier modulation schemes. In fact, N samples of the normalized input sequence

$$x_\mathrm{exp}[n] = e^{j\,2\pi\,\frac{n}{N}}, \quad N \geq 3,\ n = 1, 2, \ldots \tag{56}$$

are sufficient to obtain the exact value of α. This interesting result can be derived by starting with the distorted sequence $y[n]$

$$y[n] = e^{j\,2\pi\,\frac{n}{N}} + \alpha\, e^{-j\,2\pi\,\frac{n}{N}}. \tag{57}$$

Inserting $y[k]$ into the sample mean (53), which in this case represents a deterministic value rather than a random variable, leads to

$$\widehat{m}_2[N] = \frac{1}{N}\sum_{k=1}^{N}\left(e^{j\,2\pi\,\frac{k}{N}} + \alpha\, e^{-j\,2\pi\,\frac{k}{N}}\right)^2 = 2\alpha + \frac{1}{N}\sum_{k=0}^{N-1} e^{j\,\frac{4\pi}{N}}\left(e^{j\,\frac{4\pi}{N}}\right)^k + \sum_{k=0}^{N-1} e^{-j\,\frac{4\pi}{N}}\left(e^{-j\,\frac{4\pi}{N}}\right)^k. \tag{58}$$

Both sums represent finite geometric series. Inserting into the closed form formula for the finite geometric series immediately shows that both sums are zero for $N \geq 3$. From (58) we obtain

$$\widehat{\alpha} = \frac{\widehat{m}_2}{2} \tag{59}$$

In this derivation no noise was considered. Even in the presence of additive noise, this signal type leads to an excellent estimation accuracy. In this case the number of input samples should be a multiple of N.

C. Simulation Results

Since no simple analytical predictions can be made on the statistical properties of the moment-based estimator, only numerical simulations can show its capabilities. All performance metrics were obtained for sequences with 10^5 samples and double-precision arithmetic. White Gaussian noise and LTE-20 signals with square-type constellation and various allocation patterns have been chosen as input signals. Both signal types are zero mean and proper and therefore fulfill the assumptions made during the derivation of the estimator. Even in case of a BPSK constellation, an LTE downlink signal is still proper due to the underlying multi-carrier modulation. In the uplink, however, a BPSK signal violates the properness assumption.

Fig. 12 visualizes the simulated bias and variance for white Gaussian noise, a fully allocated LTE-20 uplink signal and a fully allocated LTE-20 downlink signal. Both LTE signals use a QPSK constellation. Within the accuracy of the simulation, the estimation is unbiased for all three signal types. Interestingly, for white Gaussian noise and the uplink signal, also the variance is the same. The variance of the downlink signal is larger by a factor of 2 in the practically relevant range of $|\alpha| < 0.2$. Bias and variance are again independent of the phase of α. For $|\alpha| = 1$, the variance is 0, indicating an exact solution.

In Fig. 13 the simulated image rejection ratio (23) over the magnitude of α is plotted for white Gaussian noise and LTE downlink signals with QPSK constellation mapping. Interestingly, and different to the estimator in Section IV, for all signals, the $\mathrm{IRR}_{\mathrm{dB}}^{\mathrm{canc}}$ is independent of α as long as $|\alpha| < 1$. Similarly to the estimator in Section IV, the achievable performance heavily depends on the allocation pattern of the used LTE signals. The power spectral density of the patterns used in the simulation is shown in Fig. 8. The allocation of a single outer resource block gives an excellent rejection of over

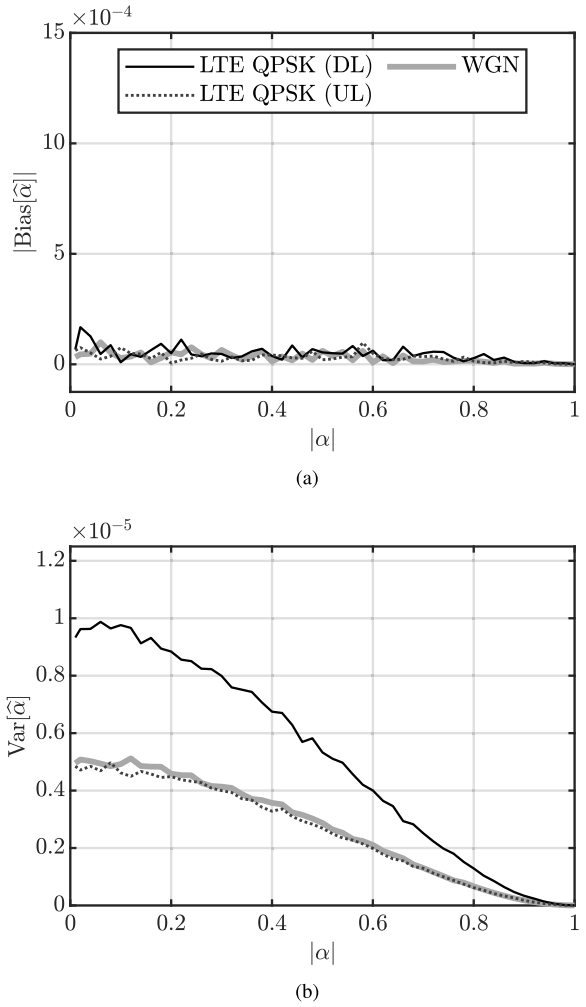

Fig. 12. Moment-based estimator: simulated bias (a) and variance (b) with white Gaussian noise and fully allocated LTE-20 up- and downlink signals (100 resource blocks).

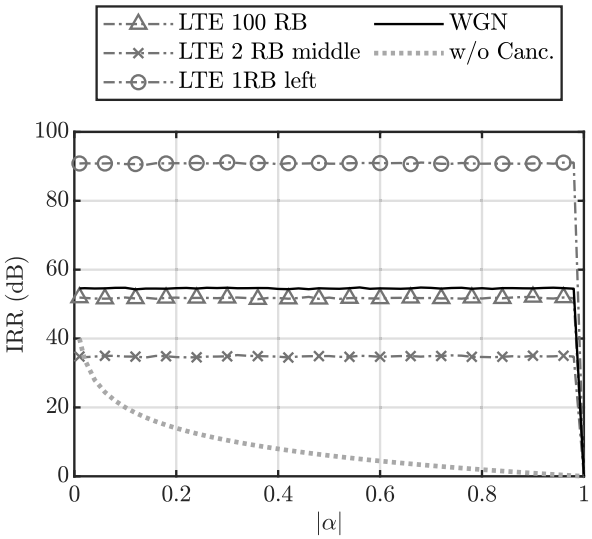

Fig. 13. Moment-based estimator: simulated image rejection ratio for white Gaussian noise and LTE-20 downlink signals with three different allocation patterns.

90 dB. For white Gaussian noise an $\mathrm{IRR}_{\mathrm{dB}}^{\mathrm{canc}}$ of about 55 dB is obtained. A fully allocated LTE-20 downlink signal leads to an $\mathrm{IRR}_{\mathrm{dB}}^{\mathrm{canc}}$ of about 52 dB. A centered narrow allocation

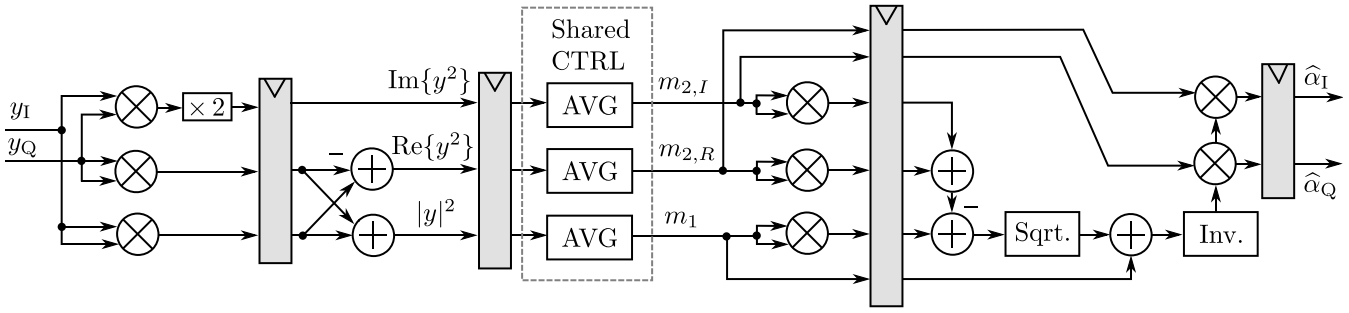

Fig. 14. Block diagram of moment-based estimator.

TABLE III
RESOURCE USAGE OF MOMENT-BASED IMBALANCE ESTIMATOR ON CYCLONE V 5CSXFC6D6F31C6 FPGA (RELATIVE USAGE IN PARENTHESIS)

	Avg. w. Shifts	Avg w. LUT
Logic Util. (in ALMs)	772 (2 %)	1087 (3 %)
Register Bits	628 (< 1 %)	763 (< 1 %)
Embedded Multipliers	8 (4 %)	11 (5 %)
F_{max} (Slow 1.1 V 85 °C)	104 MHz	69 MHz

gives the lowest $\mathrm{IRR}_{\mathrm{dB}}^{\mathrm{canc}}$ of about 35 dB, which is around 3 dB better compared to the estimator in Section IV.

D. Digital Hardware Architecture

For the second estimator we again decided to develop a fully pipelined architecture, capable of real-time processing incoming data samples. As outlined in Fig. 14, the two moments of the input signal are estimated with a direct implementation of the iterative equations (54) and (55). In a first step, $y^2 = y_\mathrm{I}^2 - y_\mathrm{Q}^2 + 2jy_\mathrm{I}y_\mathrm{Q}$ and $|y|^2 = y_\mathrm{I}^2 + y_\mathrm{Q}^2$ are computed, where only three distinct products occur. The terms y^2 and $|y|^2$ are then averaged by the iterative sample mean approximation depicted in Fig. 10. A detailed description of this unit is given in Section IV-D. Using the moments $\widehat{m}_1$ and $\widehat{m}_2$, the variance of the components of $x[n]$ is computed by inserting into (50). The required square root is approximated by a variant of the architecture shown in Fig. 11. Here, the lookup table contains the values of the square root for a normalized number range, and the exponent is divided by 2. The final estimate of the imbalance factor is obtained by computing (51). The occurring division is again approximated by the LUT based architecture visualized in Fig. 11. In total, the estimator requires 8 real multipliers and 5 adders working at the input bit width. Depending on the implementation of the averagers, these blocks might contribute 3 additional multipliers with lower bit width.

Tab. III summarizes the synthesis result of the moment-based estimator on a Cyclone V FPGA. Compared to the estimator in Section IV, the moment-based estimator requires less logic elements, but 8 or 9 additional multipliers, depending on the configuration. Therefore, if implemented on an application-specific integrated circuit (ASIC) the second estimator would have higher area and power requirements.

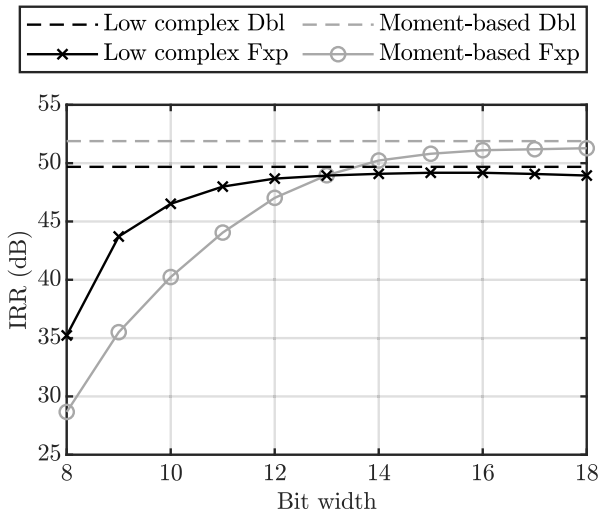

Fig. 15. Effect of fixed-point arithmetic on the estimation performance of the ultra-low complex and the moment-based estimator.

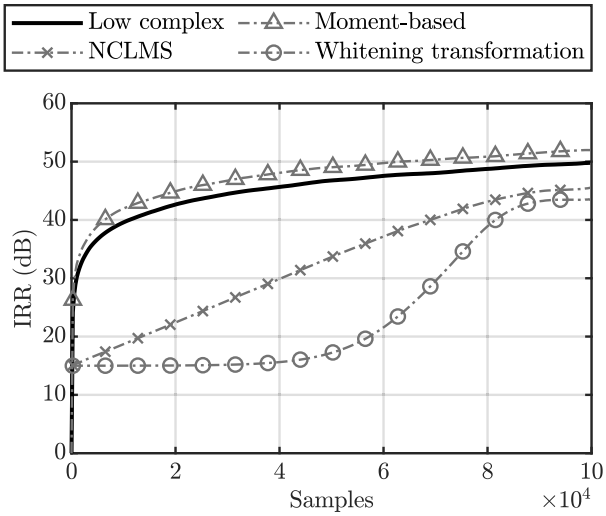

Fig. 16. Convergence behavior of selected I/Q imbalance estimation algorithms on a fully allocated LTE-20 downlink signal. Initial $\mathrm{IRR}_{\mathrm{dB}}$ is 15 dB.

VI. ESTIMATION PERFORMANCE OF FIXED-POINT IMPLEMENTATIONS

In all previous simulations only double-precision implementations of the algorithms have been considered. However, the achievable image rejection in a practical application might be significantly lower than the shown performance numbers.

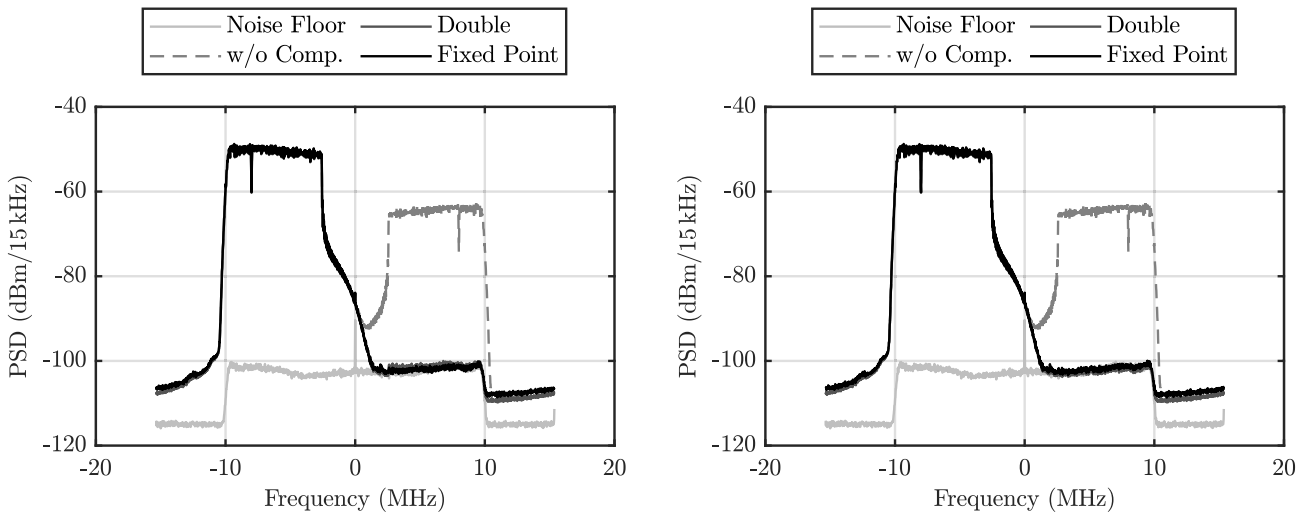

(a) Low-complexity estimator

(b) Moment-based estimator

Fig. 17. Image rejection performance of ultra-low complexity and moment-based estimator on measurement data.

One reason for the degraded estimation performance is additive noise, consisting of a sampled analog noise component and quantization noise of the ADC. In (11) this term is denoted with $w[n]$. In addition, a practical implementation in a receiver usually uses fixed-point arithmetic, which causes additional noise by truncation of intermediate results or the approximation of demanding operations such as division and square root. This component depends directly on the chosen bit widths. Consequently, we use bit-true models of the hardware architectures presented above and compare the performance to the double-precision implementations. This allows us to assess the performance loss in terms of image rejection due to fixed-point arithmetic. Fig. 15 visualizes the $\mathrm{IRR}_{\mathrm{dB}}^{\mathrm{canc}}$ for varying bit width of the main data path, while keeping the size and bit width of all LUTs constant. 10^5 samples of a fully allocated LTE-20 sequence with QPSK constellation mapping were used in the simulations. The signal-to-noise ratio of the receive signal $y[n]$ was set to 55 dB. The initial image rejection was $15dB$. Especially the moment-based estimator shows a substantial drop in image rejection for bit widths lower than 14 bit. We assume that the observed behavior is mainly caused by the cascading of multiplications and the approximated division, which both amplify the quantization noise. In contrast, the low-complexity estimator discussed in Section IV is able to almost match the double-precision implementation for bit widths down to 12 bit. Combined with its overall lower hardware requirements, this robustness makes the estimator very suitable for usage in low-cost receive chains. The additive noise component of $y[n]$ had no influence on the performance of both estimators.

VII. Comparison to Other State-of-the-Art I/Q Imbalance Estimators

Unlike the proposed ultra-low complex estimator and the moment-based approach, many state-of-the-art blind imbalance compensation algorithms iteratively update their estimate based on the feedback of the canceler output signal. A very recent example for this group of estimators is [17], where a quadratic cost function is minimized using a normalized complex least-mean squares (NCLMS) algorithm. Another example is [11], which solves a blind signal separation problem by iteratively computing a suitable whitening transformation. The conceptual differences between these classes of estimators directly affect the convergence behavior and the achievable image rejection ratio, as the simulation results in Fig. 16 illustrate. In these simulations, a fully allocated LTE-20 downlink signal was selected as wanted receive signal and the initial $\mathrm{IRR}_{\mathrm{dB}}$ was set to 15 dB. Double-precision arithmetic was used for all four algorithms. Both, the NCLMS and the whitening transformation, offer a step size parameter which was tuned for maximum $\mathrm{IRR}_{\mathrm{dB}}^{\mathrm{canc}}$ within the input sequence length of 10^5 samples. While the ultra-low complex and moment-based approach perform similarly, the other two algorithms show a significantly slower convergence and a worse final $\mathrm{IRR}_{\mathrm{dB}}^{\mathrm{canc}}$ of 50 dB.

VIII. Experimental Results

We conclude our investigations on the ultra-low complex and moment-based estimator by applying both fixed-point implementations to measurement data. For this purpose we captured digital baseband data from an integrated low-cost LTE/4G receiver. These data streams were then processed on an FPGA development board. The results, i.e. the corrected signal and the estimated imbalance factor, were sent back to the PC and visualized. As a reference, a floating-point variant of both algorithms applied to the captured data. The chosen receive signal was an LTE-20 downlink signal with a carrier frequency of 1.84 GHz and an initial IRR of about 15 dB. The used constellation mapping was QPSK. Fig. 17 visualizes the power spectral densities of the signal without imbalance cancellation and after applying both estimators. 10^5 samples were used for all estimations. In Fig. 17a, the floating-point and the fixed-point variant of the ultra-low complexity approach is applied. Fig. 17b shows the results for the floating-point and

the fixed-point variant of the moment-based approach. As a reference, both figures also contain the measured noise floor. In the first estimator, most arithmetic operations were implemented using a data format of 13 bit signed. The second estimator required a bit width of 15 bit. Compared to the input, the internal bit width of the averager was increased by 8 bit to 10 bit, depending on the estimator. The scaling sequence used inside the averagers was approximated with bit shifts only, which interestingly performs almost equal to the lookup table based variant. As Fig. 17 shows, there is only a marginal difference between the fixed-point and the floating-point implementations. Both approaches attain a final $\mathrm{IRR}_{\mathrm{dB}}^{\mathrm{canc}}$ of about 45 dB, which is the limit for the measurement data due to the receiver noise floor. The achieved image rejection ratio is in accordance with simulations that predict an $\mathrm{IRR}_{\mathrm{dB}}^{\mathrm{canc}}$ of around 47 dB.

IX. Conclusion

In this paper, we presented a novel blind ultra-low complexity algorithm for I/Q imbalance compensation in direct-conversion transceivers. This algorithm estimates the imbalance factor and can be combined with a general I/Q imbalance cancellation scheme described in this work. In contrast to many existing algorithms, the estimator does not require a feedback from the cancellation structure, and can be implemented stand-alone. An existing estimator, which also fits the shown cancellation structure, is based on the method of moments. In our work, we extended the analysis of this algorithm and compared it with the ultra-low complexity approach. We demonstrated the capabilities of both estimators with LTE up- and downlink signals for varying bandwidth allocation and modulation schemes. While in theory, the second algorithm yields a slightly better estimation performance, in a fixed-point implementation this advantage is lost due to its higher sensitivity to rounding errors. Its lower hardware requirements and higher robustness in fixed-point arithmetic render the ultra-low complex estimator more suitable for implementation. A comparison to feedback-based state-of-the-art algorithms revealed that the ultra-low complexity as well as the moment-based approach are superior in terms of adaptation rate and obtainable image rejection. We concluded our work with experimental results, where we used the presented hardware architectures of both algorithms to process the received signal from a low-cost LTE/4G transceiver on an FPGA. Both estimators succeeded in suppressing the image in the received signal down to the noise floor.

References

[1] X. Li and M. Ismail, *Multi-Standard CMOS Wireless Receivers: Analysis and Design* (The Springer International Series in Engineering and Computer Science). New York, NY, USA: Springer, 2006.

[2] S. Mirabbasi and K. Martin, "Classical and modern receiver architectures," *IEEE Commun. Mag.*, vol. 38, no. 11, pp. 132–139, Nov. 2000.

[3] B. Razavi, "Design considerations for direct-conversion receivers," *IEEE Trans. Circuits Syst. II, Analog Digit. Signal Process.*, vol. 44, no. 6, pp. 428–435, Jun. 1997.

[4] J. Crols and M. Steyaert, *CMOS Wireless Transceiver Design*. Norwell, MA, USA: Kluwer, 1997.

[5] B. Razavi, *RF Microelectronics*, 2nd ed. Upper Saddle River, NJ, USA: Prentice-Hall, 2011.

[6] A. A. Abidi, "Direct-conversion radio transceivers for digital communications," *IEEE J. Solid-State Circuits*, vol. 30, no. 12, pp. 1399–1410, Dec. 1995.

[7] Y. C. Pan and S. M. Phoong, "A time-domain joint estimation algorithm for CFO and I/Q imbalance in wideband direct-conversion receivers," *IEEE Trans. Wireless Commun.*, vol. 11, no. 7, pp. 2353–2361, Jul. 2012.

[8] G.-T. Gil, I.-H. Sohn, J.-K. Park, and Y. H. Lee, "Joint ML estimation of carrier frequency, channel, I/Q mismatch, and DC offset in communication receivers," *IEEE Trans. Veh. Technol.*, vol. 54, no. 1, pp. 338–349, Jan. 2005.

[9] L. J. Breems, E. C. Dijkmans, and J. H. Huijsing, "A quadrature data-dependent DEM algorithm to improve image rejection of a complex $\sigma\Delta$ modulator," in *IEEE ISSCC Dig. Tech. Papers*, Feb. 2001, pp. 48–49.

[10] M. Petit and A. Springer, "Analysis of a properness-based blind adaptive I/Q filter mismatch compensation," *IEEE Trans. Wireless Commun.*, vol. 15, no. 1, pp. 781–793, Jan. 2016.

[11] M. Valkama, M. Renfors, and V. Koivunen, "Blind signal estimation in conjugate signal models with application to I/Q imbalance compensation," *IEEE Signal Process. Lett.*, vol. 12, no. 11, pp. 733–736, Nov. 2005.

[12] L. Anttila, M. Valkama, and M. Renfors, "Blind moment estimation techniques for I/Q imbalance compensation in quadrature receivers," in *Proc. IEEE 17th Int. Symp. Pers., Indoor Mobile Radio Commun.*, Sep. 2006, pp. 1–5.

[13] L. Anttila, M. Valkama, and M. Renfors, "Blind compensation of frequency-selective I/Q imbalances in quadrature radio receivers: Circularity -based approach," in *Proc. IEEE Int. Conf. Acoust., Speech Signal Process. (ICASSP)*, vol. 3, Apr. 2007, pp. III-245–III-248.

[14] P. S. R. Diniz, *Adaptive Filtering: Algorithms and Practical Implementation*, 4th ed. New York, NY, USA: Springer, 2013.

[15] A. H. Sayed, *Fundamentals of Adaptive Filtering*, Hoboken, NJ, USA: Wiley, 2003.

[16] S. Lerstaveesin and B.-S. Song, "A complex image rejection circuit with sign detection only," *IEEE J. Solid-State Circuits*, vol. 41, no. 12, pp. 2693–2702, Dec. 2006.

[17] H. Cheng, Y. Xia, Y. Huang, L. Yang, and D. P. Mandic, "A normalized complex LMS based blind I/Q imbalance compensator for GFDM receivers and its full second-order performance analysis," *IEEE Trans. Signal Process.*, vol. 66, no. 17, pp. 4701–4712, Sep. 2018.

[18] L. Anttila, M. Valkama, and M. Renfors, "Gradient-based blind iterative techniques for I/Q imbalance compensation in digital radio receivers," in *Proc. IEEE 8th Workshop Signal Process. Adv. Wireless Commun.*, Jun. 2007, pp. 1–5.

[19] M. Valkama, M. Renfors, and V. Koivunen, "Advanced methods for I/Q imbalance compensation in communication receivers," *IEEE Trans. Signal Process.*, vol. 49, no. 10, pp. 2335–2344, Oct. 2001.

[20] R. S. Kanumalli *et al.*, "Digitally-intensive transceivers for future mobile communications–emerging trends and challenges," *e i Elektrotechnik und Informationstechnik*, vol. 135, no. 1, pp. 30–39, Feb. 2018.

[21] A. Gebhard, R. S. Kanumalli, B. Neurauter, and M. Huemer, "Adaptive self-interference cancelation in LTE-A carrier aggregation FDD direct-conversion transceivers," in *Proc. IEEE Sensor Array Multichannel Signal Process. Workshop (SAM)*, Jul. 2016, pp. 1–5.

[22] A. Elmaghraby *et al.*, "A mixed-signal technique for TX-induced modulated spur cancellation in LTE-CA receivers," *IEEE Trans. Circuits Syst. I, Reg. Papers*, vol. 65, no. 9, pp. 3060–3073, Sep. 2018.

[23] S. Sadjina, R. S. Kanumalli, A. Gebhard, K. Dufrêne, M. Huemer, and H. Pretl, "A mixed-signal circuit technique for cancellation of interferers modulated by LO phase-noise in 4G/5G CA transceivers," *IEEE Trans. Circuits Syst. I, Reg. Papers*, vol. 65, no. 11, pp. 3745–3755, Nov. 2018.

[24] R. S. Kanumalli *et al.*, "Mixed-signal based enhanced widely linear cancellation of modulated spur interference in LTE-CA transceivers," in *Proc. 52nd Asilomar Conf. Signals, Syst., Comput.*, Oct. 2018, pp. 1382–1388.

[25] L. Anttila, M. Valkama, and M. Renfors, "Circularity-based I/Q imbalance compensation in Wideband direct-conversion receivers," *IEEE Trans. Veh. Tech.*, vol. 57, no. 4, pp. 2099–2113, Jul. 2008.

[26] G. Xing, M. Shen, and H. Liu, "Frequency offset and I/Q imbalance compensation for OFDM direct-conversion receivers," in *Proc. IEEE Int. Conf. Acoust., Speech, Signal Process., (ICASSP).*, vol. 4, Apr. 2003, pp. IV–708.

[27] K. O. Bowman and L. R. Shenton, "Estimation: Method of moments," in *Encyclopedia of Statistical Sciences*, 2nd ed. 2006.

[28] F. D. Neeser and J. L. Massey, "Proper complex random processes with applications to information theory," *IEEE Trans. Inf. Theory*, vol. 39, no. 4, pp. 1293–1302, Jul. 1993.

[29] E. Dahlman, S. Parkvall, and J. Skold, *4G: LTE/LTE-Advanced for Mobile Broadband*. Amsterdam, The Netherlands: Elsevier, 2013.
[30] A. Papoulis, *Probability—Random Variables and Stochastic Processes*. New York, NY, USA: McGraw-Hill, 1984.
[31] P. K. Meher, J. Valls, T.-B. Juang, K. Sridharan, and K. Maharatna, "50 years of CORDIC: Algorithms, architectures, and applications," *IEEE Trans. Circuits Syst. I, Reg. Papers*, vol. 56, no. 9, pp. 1893–1907, Sep. 2009.
[32] E. Whittaker and G. Watson, *A Course of Modern Analysis* (A Course of Modern Analysis: An Introduction to the General Theory of Infinite Processes and of Analytic Functions, with an Account of the Principal Transcendental Functions). Cambridge, U.K.: Cambridge Univ. Press, 1996.

Thomas Paireder (S'19) was born in Melk, Austria, in 1992. He received the bachelor's degree (Hons.) in information electronics and the master's degree (Hons.) in electronics and information technology from Johannes Kepler University Linz (JKU), Linz, Austria, in 2016 and 2018, respectively. He is currently pursuing the Ph.D. degree in cooperation with DMCE GmbH (Intel Linz), Linz, with a focus on receiver interference cancellation by means of adaptive signal processing methods. His master's thesis was focused on signal processing in cooperation with the Research Center for Nondestructive Testing GmbH. In his thesis, he implemented a real-time processing system for laser-ultrasonic signals.

From 2012 to 2018, he was with JKU. Since 2018, he has been a member of the Institute of Signal Processing, JKU.

Christian Motz (S'17) was born in Vöcklabruck, Austria, in 1990. He received the bachelor's degree (Hons.) in hardware software design and the master's degree in embedded systems design from the School of Informatics, Communications and Media, University of Applied Sciences Upper Austria, Hagenberg, Austria, in 2013 and 2015, respectively. He is currently pursuing the Ph.D. degree with the Institute of Signal Processing, Johannes Kepler University Linz (JKU), Linz, Austria, in cooperation with DMCE GmbH (Intel Linz), Linz. His master's thesis was focused on pattern matching cooperation with the Software Competence Center Hagenberg GmbH, Hagenberg. His thesis was on efficient implementation of Weyls discrepancy measure for 2-D image data.

From 2010 to 2015, he was with the University of Applied Sciences Upper Austria. In 2016, he joined the Research Center or Non Destructive Testing GmbH, Linz. Since 2017, he has been a member of the Institute of Signal Processing, JKU, and the CD Laboratory for Digitally Assisted RF Transceivers for Future Mobile Communications, where he is involved in receiver interference cancellation by means of adaptive signal processing methods.

Ram S. Kanumalli was born in Guntur, India. He received the Dipl.Ing. (M.Sc.) degree in information technology from the Alpen-Adria-Universität (AAU), Klagenfurt, Austria, in 2012, with a focus on embedded communications and signal processing field. He is currently pursuing the Dr.Ing. (Ph.D.) degree with the Institute of Signal Processing, Johannes Kepler University (JKU), Linz, Austria.

From 2013 to 2015, he was a Research Assistant with the Institute of Signal Processing, JKU. Since 2016, he has been with Intel Linz, Austria. In 2012, he was a Research Assistant with the Communications and Signal Processing Group, AAU. His research activities focus on the study and development of digital interference cancellation techniques in the presence of various RF imperfections for the next-generation wireless transceiver systems.

Silvester Sadjina (S'16) was born in Salzburg, Austria, in 1988. He received the B.S. and M.S. degrees in information electronics from Johannes Kepler University (JKU), Linz, Austria, in 2013 and 2015, respectively. He is currently pursuing the Dr.Ing. (Ph.D.) degree with the Institute of Integrated Circuits, JKU, in cooperation with Danube Mobile Communications Engineering (DMCE) GmbH & Co KG (majority owned by Intel Austria GmbH), Linz. In his studies, he specialized in measurement technology and communication engineering.

In 2014, he was a Research Assistant with the Institute for Measurement Technology, JKU. His research activities focus on the study and the development of mixed signal interference cancellation techniques for the mitigation of RX performance degradation in cellular transceiver systems.

Mario Huemer (M'00–SM'07) was born in Wels, Austria, in 1970. He received the Dipl.Ing. degree in mechatronics and the Dr.Techn. degree from Johannes Kepler University (JKU) Linz, Austria, in 1996 and 1999, respectively.

From 1997 to 2000, he was a Research Assistant with the Institute for Communications and Information Engineering, JKU Linz. From 2000 to 2002, he was a Project Manager with the Research and Development Center for Wireless Products, DICE Linz GmbH (an Infineon subsidiary). He was a Lecturer with the University of Applied Sciences of Upper Austria from 2002 to 2004, an Associate Professor of electronics engineering with the University of Erlangen-Nuremberg, Germany, from 2004 to 2007, and a Full Professor of embedded systems and signal processing with Klagenfurt University, Austria, from 2007 to 2013. From 2012 to 2013, he was the Dean of the Faculty of Technical Sciences. In 2013, he moved back to Linz, where he is currently heading the Institute of Signal Processing, JKU Linz, as a Full Professor. Since 2017, he has been the Co-Head of the Christian Doppler Laboratory for Digitally Assisted RF Transceivers for Future Mobile Communications. His research focuses on statistical and adaptive signal processing, signal processing architectures and implementations, as well as mixed signal processing with applications in information and communications engineering, radio frequency and baseband integrated circuits, and sensor and biomedical signal processing. Within these fields, he has published more than 230 scientific papers.

Dr. Huemer is also a member of the IEEE Signal Processing Society, the IEEE Circuits and Systems Society, the IEEE Communications Society, and the IEEE Microwave Theory and Techniques Society. He is also member of the German Society of Information Technology (ITG) and the Austrian Electrotechnical Association (OVE).